Materials Advances

ROYAL SOCIETY OF CHEMISTRY

PAPER

View Article Online
View Journal

Cite this: DOI: 10.1039/d6ma00355a

Degradation or adsorption? Revisiting organic dye removal by two morphologies of $InVO_4$

Hassan Esmaili, *[a] Roozbeh Izadi, [a] Amirhossein Ahmadnezhad,[a] Astita Dubey, [ab] Marianela Escobar-Castillo [a] and Doru. C. Lupascu *[a]

Indium vanadate ($InVO_4$) has attracted considerable attention for photocatalytic applications owing to its narrow band gap, non-toxicity, and high chemical stability. However, for the removal of organic dyes from wastewater, both photocatalytic degradation and adsorption by $InVO_4$ have been reported, and the dominant mechanism remains unclear. This study investigates the removal mechanism of cationic dyes by $InVO_4$. Two distinct morphologies of $InVO_4$, spherical (IVO-S) and nanorod (IVO-R), were synthesized *via* a hydrothermal method. Comparative removal tests under light and dark conditions suggest that adsorption, rather than photocatalytic degradation, is the dominant removal pathway under the conditions investigated. Among the two morphologies, IVO-R exhibits superior adsorption performance, achieving a maximum capacity of 290 mg g^{-1} for methylene blue (MB). This is attributed to its smaller particle size. The material demonstrates excellent pH tolerance, maintaining high adsorption efficiency across a broad pH range (2–10), with an optimal dosage of 0.15 g L^{-1}. Zeta potential analysis confirms a negatively charged surface within this pH range. Adsorption was significant only for cationic dyes, suggesting electrostatic attraction as the key driving force. Furthermore, XPS analysis reveals no evidence of strong chemical bonding between MB and the $InVO_4$ surface, implying that non-covalent interactions between MB and $InVO_4$ surface sites underpin the adsorption process. Kinetic studies indicate that adsorption follows a pseudo-second order model, with a rate constant (k_2) of 0.009 g mg^{-1} min^{-1} for 30 mg L^{-1} MB. Isotherm analysis shows the best fit with the Sips model predicting a maximum adsorption capacity of 285 mg g^{-1}, closely matching the experimental results.

Received 13th March 2026,
Accepted 15th May 2026

DOI: 10.1039/d6ma00355a

rsc.li/materials-advances

1. Introduction

Given the widespread use of synthetic dyes in textiles, cosmetics, printing, and plastics, along with their chemical stability due to complex structures containing auxochromes and chromophores, they are resistant to natural degradation. Therefore, it is crucial to develop and implement efficient methods for their removal from aquatic environments.[1,2] To address the environmental challenges caused by synthetic dyes, various methods have been employed to remove them from water sources. These methods are generally categorized into three main types: biological, chemical, and physical.[2,3]

Biological methods are considered conventional; however, they are often ineffective for treating wastewater with low dye concentrations.[2] In such cases, chemical methods (*e.g.*, advanced oxidation processes[4,5] and photochemical treatments[6,7]) and physical methods (*e.g.*, adsorption,[8,9] coagulation,[10,11] and flocculation[12]) are more practical and efficient. Among the available dye removal techniques, photochemical degradation and physical adsorption have demonstrated particularly promising performance in removing dyes from wastewater.[13]

The photochemical method is a chemical approach in which dyes are degraded through the application of a light source and a photocatalyst that becomes activated upon light exposure.[14] While this method effectively breaks down dye molecules, it often results in the formation of by-products, which is a notable drawback. These by-products should be subsequently removed from the solution to prevent secondary pollution.[15] However, a key advantage of photochemical treatment is the reusability of the photocatalysts, as dyes can adsorb, degrade, and desorb from their surfaces over multiple cycles.[16] In contrast, adsorption is a physical dye removal method where dye molecules adhere directly to the surface of an adsorbent *via* covalent or non-covalent interactions, including electrostatic attraction, hydrogen bonding, van der Waals forces, hydrophobic interactions, and/or π-related interactions, depending on the surface

[a] *Institute for Materials Science and Center for Nanointegration Duisburg-Essen (CENIDE), University of Duisburg-Essen, 45141 Essen, Germany. E-mail: hassan.Esmaili@stud.uni-due.de, doru.lupascu@uni-due.de*

[b] *Institute for Advanced Materials and Manufacturing, Department of Materials Science and Engineering, The University of Tennessee Knoxville, Knoxville, Tennessee 37996, USA*

chemistry of the adsorbent and the molecular structure of the dye. For aromatic dyes, π–π stacking may occur, when the adsorbent contains graphitic or conjugated aromatic domains, or between adsorbed dye molecules themselves.[17] This technique does not generate any by-products, and dyes are completely removed from the solution.[18] Nevertheless, its main limitation lies in the limited number of adsorption sites available on the adsorbent material, which restricts its capacity and reusability.

A wide range of adsorbent materials have been investigated for dye removal, including conventional adsorbents such as activated carbon, carbon nanotubes, and clays, as well as bio-based materials like lignin and advanced metal oxides such as titanium dioxide and zinc oxide.[19] These adsorbent materials offer high specific surface areas, enabling efficient dye uptake through physical adsorption mechanisms. In addition to adsorption, various photocatalytic materials have been proposed for dye degradation and photochemical dye removal, including metal oxides, metal sulfides, perovskites, and metal vanadates.[20,21] Among them, $InVO_4$, a low-bandgap semiconductor that can be activated under visible-light irradiation, has attracted attention as a promising photocatalyst for dye degradation.[22]

Interestingly, in the case of rhodamine B and methylene blue removal, both photocatalytic degradation[23–32] and adsorption[33,34] by $InVO_4$ for a similar concentration of dyes have been reported, suggesting that this material can simultaneously function as a photocatalyst and an adsorbent. For the same dye concentration range of 5–50 mg L^{-1}, both adsorption and photocatalytic degradation have been reported. These findings appear contradictory, making the role of light activation unclear. Typically, in a photocatalytic degradation process, dye molecules are first adsorbed onto the surface of the photocatalyst until adsorption–desorption equilibrium is reached; subsequently, the remaining dye molecules are degraded *via* photocatalytic reactions under light irradiation. In the case of $InVO_4$, a high adsorption capacity has been reported,[33,34] indicating that the material is capable of adsorbing nearly all dye molecules within the concentration range of 5–50 mg L^{-1} before equilibrium is achieved.

This raises a critical question: are rhodamine B and methylene blue removed from wastewater by $InVO_4$ primarily through photocatalytic degradation or *via* physical adsorption? The aim of the present study is to address this question and determine whether the removal process is truly photochemical, driven by light and $InVO_4$ as a low-bandgap photocatalyst, or whether it is predominantly an adsorption process occurring on the surface of $InVO_4$. The removal behavior of RhB and MO, representing cationic and anionic dyes, respectively, was compared under both light and dark conditions. This approach allows the effect of light irradiation to be evaluated and enables assessment of the potential contribution of a hybrid adsorption–photocatalytic process to the overall dye removal by $InVO_4$.

In addition, previous studies have reported both adsorption and photocatalytic degradation of dyes by $InVO_4$ with different morphologies. Because these morphologies are typically synthesized using various precursors and exhibit distinct surface areas, crystallinities, and related physicochemical properties, the dye removal behavior may depend on morphology. To examine this assumption, $InVO_4$ powders with two of the most commonly reported morphologies (spherical and nanorod) were synthesized in this study. By systematically comparing their dye removal behavior under identical conditions, this work also aims to clarify whether the dye removal mechanism of $InVO_4$ is morphology dependent or not. The underlying removal mechanisms are also systematically studied using dye-selectivity tests, zeta potential, FTIR, XPS, kinetic modeling, and adsorption isotherm analysis.

2. Experimental

2.1. Materials

Analytical-grade chemicals, including $NaVO_3$ (99.9%), $In(NO_3)_3{\cdot}xH_2O$ (99.9%), rhodamine B, methylene blue (MB), and methyl orange (MO), were obtained from Sigma-Aldrich. $InCl_3$ (99.995%) was sourced from Thermo Fisher Scientific. All reagents were used as received without additional purification. Aqueous solutions were prepared using ultra-pure deionized (DI) water.

2.2. Synthesis of $InVO_4$ – spherical morphology

To synthesize 1 g of $InVO_4$ with a spherical morphology, $In(NO_3)_3{\cdot}xH_2O$ and $NaVO_3$ were used as precursors. Initially, 0.47 g of $NaVO_3$ was dissolved in 150 mL of deionized (DI) water at 70 °C. After complete dissolution, the solution was cooled and maintained at 35 °C (designated as Solution A). Separately, 1.20 g of $In(NO_3)_3{\cdot}xH_2O$ were dissolved in 25 mL of DI water at room temperature (Solution B). Both solutions were stirred vigorously until fully transparent. Solution B was then added dropwise to Solution A using a pipette, resulting in the formation of a yellow/orange suspension. The mixture was stirred for 30 min to ensure homogeneity and then transferred to a 250 mL Teflon-lined stainless-steel autoclave and heated at 120 °C for 12 h. The resulting product was washed repeatedly with DI water to achieve high purity and dried at 80 °C for 12 h.

2.3. Synthesis of $InVO_4$ – nanorod morphology

For the preparation of 1 g of $InVO_4$ with nanorod morphology, $InCl_3$ and $NaVO_3$ were used as precursors, following a previously reported method.[34] Initially, 0.53 g of $NaVO_3$ were dissolved in 150 mL of deionized (DI) water at 70 °C. After complete dissolution, the solution was cooled and maintained at 35 °C (Solution A). Separately, 0.96 g of $InCl_3$ were dissolved in 25 mL of DI water at room temperature (Solution B). Both solutions were stirred vigorously until fully transparent. Solution B was then added dropwise to Solution A using a pipette, resulting in an orange suspension. The mixture was stirred for 30 min to ensure homogeneity, after which the pH was adjusted to 1.6–1.8 by adding 2 M HNO_3, producing a yellowish transparent solution. This solution was transferred to a 250 mL Teflon-lined stainless-steel autoclave and heated at

Table 1 Sample codes and their corresponding naming

Morphology	Code
Spherical	IVO-S
Nanorod	IVO-R

180 °C for 18 h. The resulting product was washed repeatedly with DI water to achieve high purity and dried at 80 °C for 12 h.

The synthesized $InVO_4$ powders with spherical and nanorod morphologies are designated by the sample codes listed in Table 1.

2.4. Characterization

The structural properties of the samples were examined by X-ray powder diffraction (XRD) using an Empyrean Series 2 diffractometer (PANalytical) equipped with a Cu K_α radiation (λ = 1.54 Å) source. Morphologies were characterized by scanning electron microscopy (SEM) with a Philips XL 30 ESEM instrument. A JEOL JEM-2100 LaB_6 TEM was operated at 200 kV for imaging. For sample preparation, a small amount of the dispersed aqueous solution was dropped onto a carbon-coated copper grid and allowed to dry at room temperature beforehand. Surface chemical states and elemental composition were analyzed by X-ray photoelectron spectroscopy (XPS). The optical absorption characteristics were determined using a UV-Visible spectrophotometer (Shimadzu UV-2600). Additionally, Fourier-transform infrared (FTIR) spectra were recorded in the ATR mode using an ALPHA Platinum spectrometer (Bruker). The zeta potential (surface charge) of the samples was measured using a Stabino I instrument (Colloid Metrix, Meerbusch, Germany). To change the pH for measuring zeta potential, HNO_3 (0.2 M) and NaOH (0.1 M) were used as acidic and basic agents, respectively.

2.5. Experimental procedure

2.5.1. Photocatalytic experiments. Rhodamine B (RhB) and methyl orange (MO) were used as model dyes to evaluate the photocatalytic activity of the IVO-R sample under visible light. The experiments were conducted in a batch photoreactor equipped with a solar-light simulator consisting of three commercial full-spectrum LED panels (300 W), positioned around the solution. Typically, 50 mL of an aqueous suspension containing 0.1 g L^{-1} of the IVO-R powder and 5 mg L^{-1} of the dye was prepared. At designated time intervals (0, 5, 30, 60, 90, 120, and 180 minutes), 1 mL of the solution was extracted and centrifuged at 7500 rpm for 30 minutes. The resulting supernatant was collected for further analysis.

2.5.2. Adsorption experiments. Methylene blue (MB), rhodamine B (RhB), and methyl orange (MO) were employed as model dyes to evaluate the adsorption performance of the as-synthesized IVO-S and IVO-R samples. Adsorption experiments were conducted in 200 mL and 100 mL glass beakers under ambient conditions in the dark. In a typical procedure, 100 mL and 50 mL of the dye solutions with varying concentrations were mixed with different amounts of IVO-S or IVO-R as adsorbents and stirred at 500 rpm. At predetermined time intervals, 1 mL of the solution was withdrawn, centrifuged at 7500 rpm for 30 minutes. The supernatant was collected for subsequent analysis.

2.5.2.1. Effect of the adsorbent dosage. To assess the influence of adsorbent dosage on dye removal, 100 mL of MB solution (40 mg L^{-1}) was used as the model system. Various amounts of IVO-R (0.05, 0.10, 0.15, 0.20, and 0.25 g L^{-1}) were added, and the adsorption capacity corresponding to each dosage was calculated and compared using eqn (1).

$$q_e = \left(\frac{C_0 - C_e}{m}\right) V \quad (1)$$

Here, C_0 and C_e (mg L^{-1}) represent the initial and equilibrium dye concentrations in solution, m denotes the mass of the adsorbent (IVO-R) in grams, and V is the solution volume in liters (L).

2.5.2.2. Effect of pH. The effect of pH on adsorption was investigated using 100 mL of MB solution (20 mg L^{-1}) containing IVO-R at an optimized dosage of 0.15 g L^{-1}. Experiments were conducted at pH values of 2, 5.5, 7, and 10 to determine the influence of pH on adsorption performance and identify optimal conditions. The pH was adjusted using 1 M NaOH and 2 M HNO_3 as basic and acidic agents, respectively. The amount of MB adsorbed per unit mass of IVO-R (q_e in mg g^{-1}) and the removal efficiency were calculated using eqn (1) and (2).

$$\text{Removal } (\%) = \left(\frac{C_0 - C_e}{C_e}\right) \times 100 \quad (2)$$

where, C_0 and C_e (mg L^{-1}) denote the initial and equilibrium dye concentrations in the solution, respectively.

2.5.2.3. Kinetic study of dye adsorption. Adsorption kinetics were evaluated by dispersing IVO-R powder (0.15 g L^{-1}) in 100 mL of MB solutions with initial concentrations of 30 mg L^{-1} and 50 mg L^{-1}. The suspensions were stirred at 500 rpm on a magnetic stirrer under ambient conditions. At predetermined time intervals (0, 5, 15, 30, 45, 60, 90, 120, 180, 240, 300, 360, 420, 480, 540, and 1440 min), 1 mL aliquots were withdrawn, centrifuged, and the supernatant was analyzed using a UV–Vis spectrophotometer to determine MB concentration. The adsorption capacity at time t (q_t) was calculated using eqn (3), and q_t *versus* time was plotted for kinetic analysis. The adsorption data were fitted to pseudo-first-order (PFO)[35] and pseudo-second-order (PSO)[36] kinetic models, and the corresponding rate constants (k_1 and k_2) were obtained using eqn (4) and (5).

$$q_t = \left(\frac{C_0 - C_t}{m}\right) V \quad (3)$$

$$q_t = q_e(1 - e^{-k_1 t}) \quad (4)$$

$$q_t = \frac{q_e^2 k_2 t}{1 + q_e k_2 t} \quad (5)$$

In these equations, q_e and q_t (mg g^{-1}) represent the adsorption capacities at equilibrium and at time t, respectively, while

k_1 (min^{-1}) and k_2 (g mg^{-1} min^{-1}) denote the rate constants for the PFO and PSO kinetic models.

2.5.2.4. Adsorption Isotherms. Adsorption isotherm experiments were conducted under optimized conditions (pH = 5.5, adsorbent dosage = 0.15 g L^{-1}) using 100 mL of MB solutions with varying initial concentrations (10, 20, 30, 40, 50, and 60 mg L^{-1}). The equilibrium adsorption capacity q_e (mg g^{-1}) was plotted against the equilibrium concentration C_e (mg L^{-1}), and the data were fitted to three isotherm models: Langmuir (eqn (6)),[37] Freundlich (eqn (7)),[38] and Sips (eqn (8)),[39] using their respective non-linear forms as follows:

$$q_e = \frac{bC_e q_m}{1 + bC_e} \quad (6)$$

$$q_e = K_F C_e^{\frac{1}{n}} \quad (7)$$

$$q_e = \frac{q_m K_S C_e^{\frac{1}{n}}}{1 + K_S C_e^{\frac{1}{n}}} \quad (8)$$

In these models, q_e (mg g^{-1}), C_e (mg L^{-1}) and q_m (mg g^{-1}) represent the equilibrium adsorption capacity, the equilibrium dye concentration, and the maximum adsorption capacity, respectively. The Langmuir constant is denoted by b (L mg^{-1}). For the Freundlich model, K_F (mg g^{-1})(L mg^{-1})$^{1/n}$ and n (g L^{-1}) are the equilibrium constant and heterogeneity factor, respectively. In the Sips model, K_S (L mg^{-1}) indicates the adsorption affinity constant.

2.5.3. Characterization of aqueous phase products. The degradation of RhB, MB, and MO was monitored using a UV–Vis spectrophotometer (Shimadzu UV-2600) by tracking changes in their characteristic absorption peaks. Specifically, the maximum absorbance at 554 nm, 664 nm, and 464 nm was recorded for RhB, MB, and MO, respectively. According to Beer–Lambert's law, the solution concentration is directly proportional to absorbance.[40] Therefore, the normalized concentration ratio (C_t/C_0) at time t corresponds to the normalized absorbance ratio (A_t/A_0), where A_0 and A_t represent the absorbance at the initial time and at time t, and C_0 and C_t denote the corresponding dye concentrations.[41,42]

3. Results and discussion

Fig. 1 shows the XRD patterns of the IVO-S and IVO-R samples synthesized *via* the hydrothermal method using different indium precursors. For the IVO-S sample, $In(NO_3)_3{\cdot}xH_2O$ was used, whereas $InCl_3$ was employed for the IVO-R sample. The XRD patterns confirm the successful synthesis of both samples, as they can be indexed to the reference pattern of $InVO_4$ (JCPDS No. 98-015-5162). Both samples exhibit an orthorhombic crystal structure with the *Cmcm* (No. 63) space group. The main diffraction peaks appear at 18.58°, 20.82°, 23.02°, 24.88°, 31.05°, 33.10°, and 35.18°. Although the two samples share similar crystal structures, differences in peak intensities indicate variations in crystallinity. The IVO-S sample, with higher

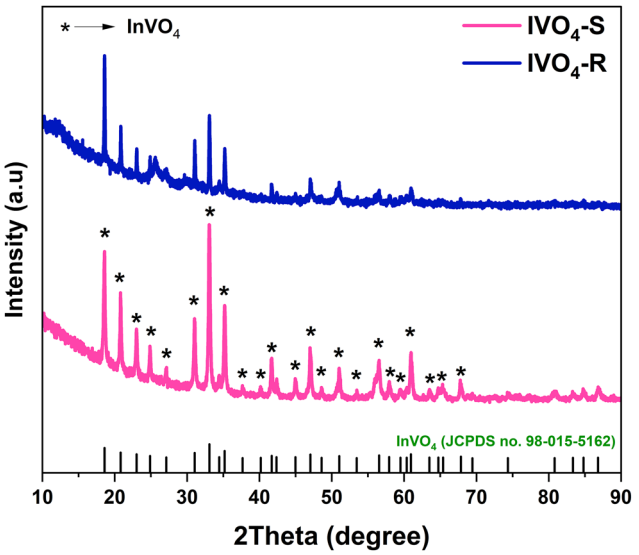

Fig. 1 XRD patterns of IVO-S and IVO-R samples using Rietveld refinement (goodness of fits: 1–1.5).

peak intensities, demonstrates a greater degree of crystallinity compared to IVO-R. Notably, the strongest peak for IVO-S occurs at 33.10°, consistent with the reference pattern, whereas for IVO-R, the maximum peak shifts to 18.58°. This shift may be attributed to the one-dimensional structure of IVO-R compared to the three-dimensional structure of IVO-S.

As discussed, both samples exhibit similar crystal structures, with only minor differences related to crystallinity and XRD peak intensities. The most significant distinction between the two samples lies in their morphology. Fig. 2 presents the morphology and particle size distribution of the IVO-S and IVO-R samples. As shown in Fig. 2(a), the IVO-S sample, synthesized using indium nitrate as the precursor, displays a spherical morphology with particle sizes in the micrometer range (~1–4 μm). In contrast, the IVO-R sample, prepared using $InCl_3$, exhibits a rod-like structure. SEM analysis (Fig. 2(b)) suggests that IVO-R consists of nanosheets. However, high-resolution TEM images at higher magnifications (Fig. 2(c) and (d)) reveal that these nanosheets are actually agglomerates of IVO nanorods. This indicates that the use of $InCl_3$ as the precursor restricts particle growth in three dimensions, favoring one-dimensional growth and resulting in nanorod formation. Interestingly, despite being synthesized at a higher temperature and for a longer reaction time (180 °C, 18 h) compared to those of IVO-S (120 °C, 12 h), the IVO-R sample exhibits smaller particle sizes. Its rod-shaped morphology provides a larger surface area, which is advantageous for adsorption processes. As shown in the insets of Fig. 2(a) and (d), the average particle size of IVO-S is approximately 2 μm, whereas the width of IVO-R rods is below 30 nm, confirming their significantly smaller size and higher surface area.

Fig. 3(a) shows the FTIR spectra of the IVO-S and IVO-R samples. For IVO-S, four major absorption bands are observed at 446, 669, 900, and 1625 cm^{-1}, while the main peaks for IVO-R

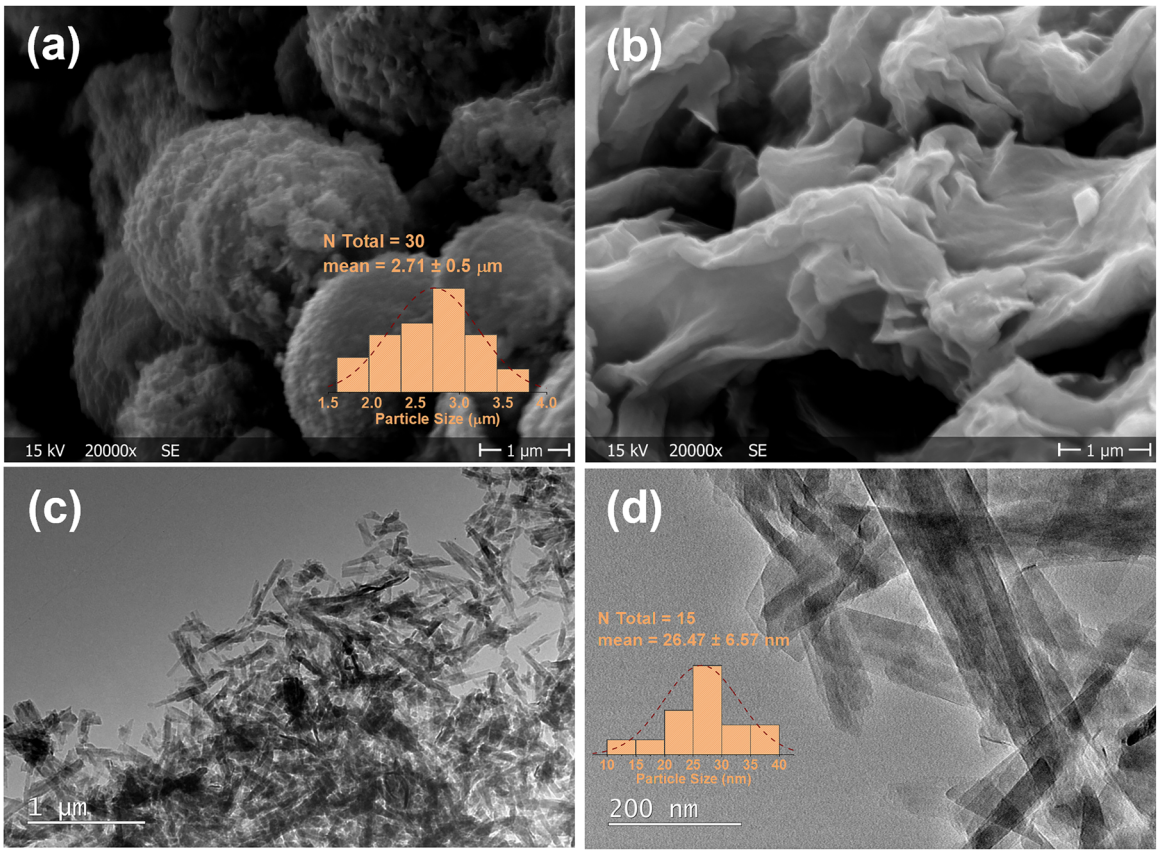

Fig. 2 SEM images of (a) IVO-S and (b) IVO-R, and (c) and (d) HRTEM images of IVO-R samples.

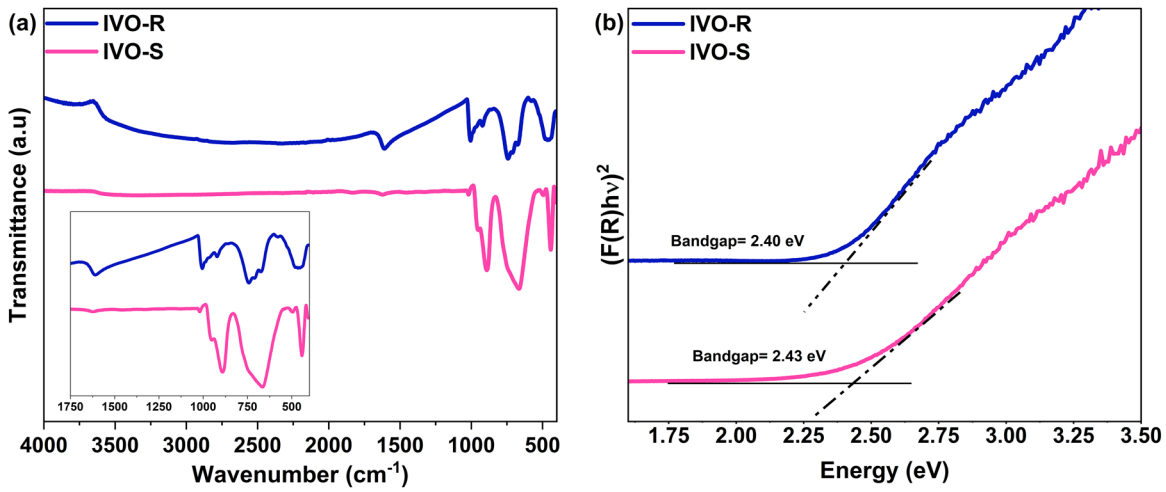

Fig. 3 FTIR spectra of (a) IVO-S and IVO-R samples and (b) the Tauc plot of IVO-S and IVO-R samples with an error of 0.03 eV.

appear at 468, 746, 1000, and 1612 cm^{-1}. In both samples, the bands near 1612–1625 cm^{-1} correspond to lattice water molecules incorporated during the hydrothermal synthesis process.[34] The peaks at 446 cm^{-1} (IVO-S) and 468 cm^{-1} (IVO-R) are attributed to the symmetric stretching vibrations of V–O–V bonds, which are characteristic of vanadate-based structures. Additionally, bending vibrations of V–O–In bonds are evident at 669 cm^{-1} for IVO-S and 746 cm^{-1} for IVO-R.[43] The band at 900 cm^{-1} in IVO-S is associated with the asymmetric stretching vibration of V–O bonds, whereas the peak at 1000 cm^{-1} in IVO-R corresponds to the stretching vibration of terminal vanadium-oxygen bonds (V═O).[44,45]

To evaluate the optical properties of $InVO_4$ and determine its light activation potential, the bandgap energy (E_g) of both samples was calculated using the Kubelka–Munk equation (eqn (9)):[46]

$$(F(R)h\nu)^{1/n} = A(h\nu - E_g) \quad (9)$$

where $F(R)$ is the Kubelka–Munk function, h is Planck's constant, ν is the light frequency, A is the equation constant, and E_g is the bandgap energy. As shown in Fig. 3(b), the bandgaps of both samples fall within the visible-light region, indicating that they can theoretically be activated under visible-light irradiation. The calculated bandgap values are 2.43 eV for IVO-S and 2.40 eV for IVO-R, showing only a negligible difference. This suggests that the synthesis conditions and particle size have little influence on the bandgap. Based on these results and the Tauc plots, both samples are suitable for photocatalytic dye degradation under visible-light illumination.

In addition, XPS analysis was employed to investigate the oxidation states and surface chemical compositions of both samples. As shown in Fig. 4, both samples exhibit similar XPS peaks. Two peaks at 445.1 and 452.6 eV correspond to In $3d_{3/2}$ and $3d_{5/2}$, confirming the presence of the In^{3+} oxidation state. The formation of V^{5+} is indicated by peaks at 517.3 and 524.9 eV, which are attributed to V $2p_{1/2}$ and V $2p_{3/2}$, respectively.

For oxygen, a slight difference is observed between the IVO-R and IVO-S samples. While both samples display a characteristic peak at 530.2 eV (530.7 eV for IVO-S), corresponding to the O^{2-} oxidation state of the lattice and surface-adsorbed oxygen, the IVO-S sample shows an additional small peak at 531.9 eV, which can be associated with the formation of hydroxyl groups on the surface.[47,48] So, based on the XPS analysis, both samples exhibit similar surface structures with identical oxidation states and chemical compositions.

To assess the light activation of $InVO_4$ for dye removal, two experiments were conducted using IVO-R as the adsorbent and rhodamine B (RhB) as the model dye. A suspension containing 0.1 g L^{-1} of IVO-R and 5 mg L^{-1} of RhB was tested under two conditions: in the dark (Fig. 5a) and under light irradiation (Fig. 5b). As shown in Fig. 5, both experiments yield identical results, indicating that light irradiation does not influence dye removal. The primary mechanism is adsorption rather than photocatalytic degradation. Approximately 55% of RhB was adsorbed within 180 min under both conditions, with most adsorption occurring within the first 5 min. This rapid adsorption can be attributed to the negative surface charge of IVO-R, confirmed by zeta potential measurements across the pH range (2–10) (see Fig. 6e). Since RhB is a cationic dye,[49] electrostatic interactions drive its adsorption onto the IVO-R surface.

Similar experiments were performed for methylene blue (MB) and methyl orange (MO) under dark conditions (0.1 g L^{-1} IVO-R and mg L^{-1} dye concentration). Fig. 5(c) and (d) show the adsorption profiles. IVO-R exhibited excellent adsorption performance for MB, achieving complete removal within 30 min. In contrast, MO adsorption was negligible, with only 5% removal. MO removal under light irradiation is also shown in Fig. S1, which shows the same results as the sample without light irradiation, indicating the poor photocatalytic activity of $InVO_4$ even when its surface is not covered by MO molecules. These results suggest the electrostatic nature of the adsorption process: MB, being cationic,[50] shows strong affinity for the negatively charged IVO-R surface, whereas MO, an anionic dye,[51] exhibits poor adsorption. Since $InVO_4$ shows adsorption rather than photocatalytic degradation in dye removal, the subsequent discussion focuses on its adsorption efficiency, evaluating the effect of adsorption parameters, and

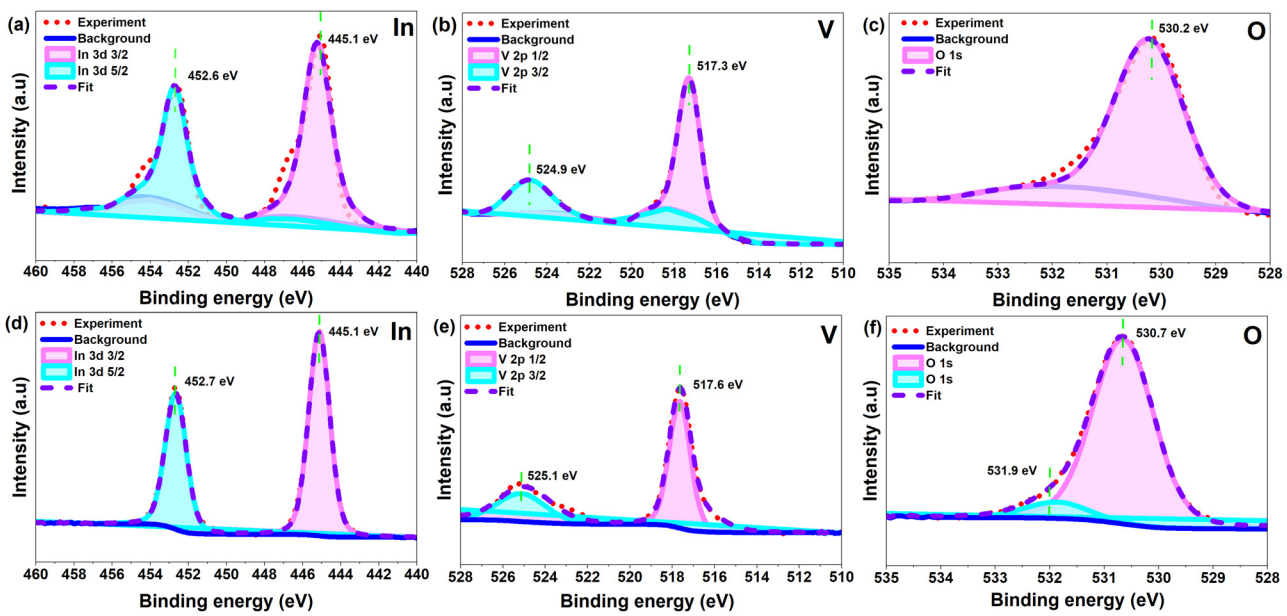

Fig. 4 XPS analysis of the $InVO_4$ samples: (a)–(c) In, V, and O scan spectra for the IVO-R sample and (d)–(f) In, V, and O scan spectra for the IVO-S sample.

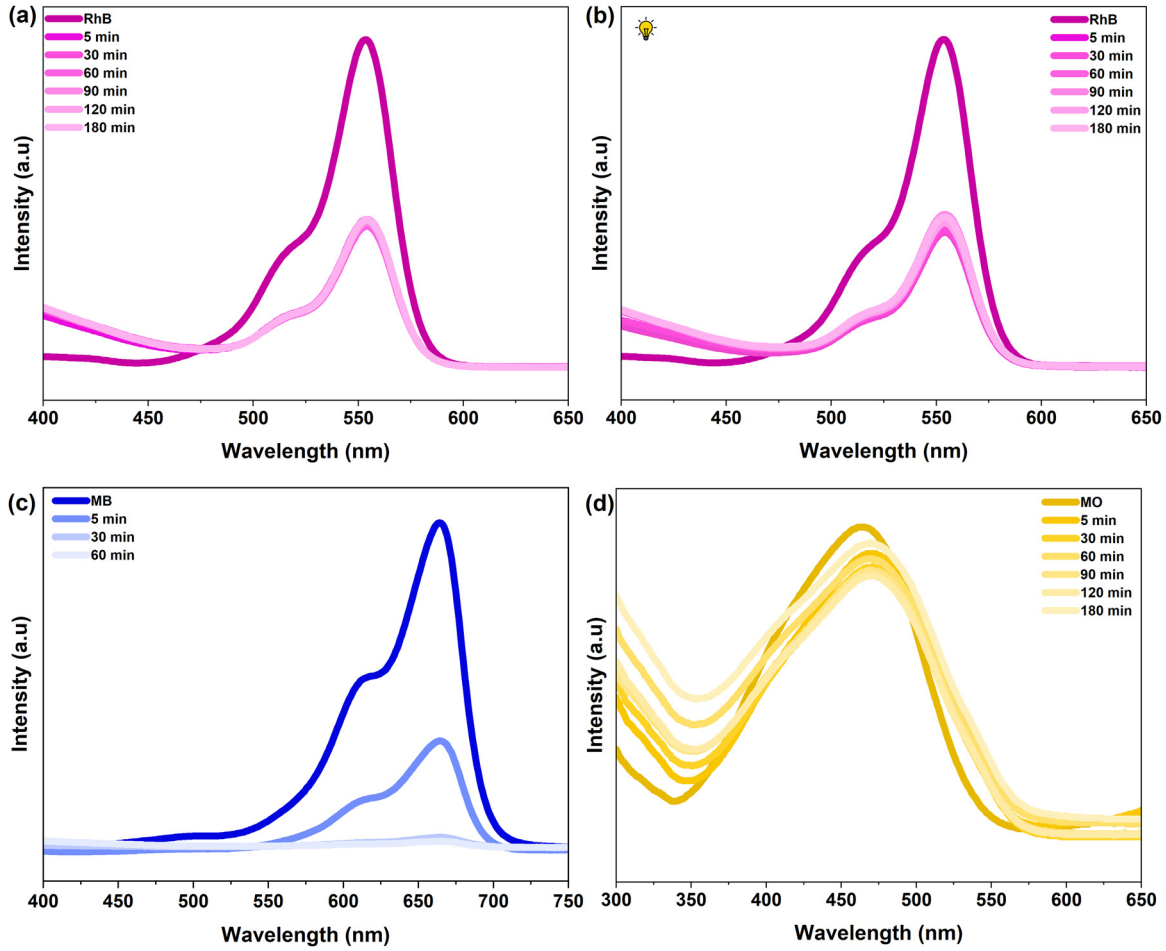

Fig. 5 UV-Vis spectra of (a) rhodamine B without light in the dark, (b) rhodamine B with light irradiation, (c) methylene blue in the dark, and (d) methyl orange in the dark using IVO-R sample at different time intervals (IVO-R dosage: 0.1 g L^{-1}, dye concentration 5 mg L^{-1}).

presents kinetic and isotherm studies and a comparative analysis with conventional adsorbents.

To explore the adsorption capacity of $InVO_4$ and identify strategies for its optimization, morphology was selected as the first parameter for investigation. Two distinct morphologies, spherical and rod-shaped, were evaluated for methylene blue (MB) adsorption. In a typical test, IVO-R and IVO-S powders (0.1 g L^{-1}) were added to a 5 mg L^{-1} MB solution, and the dye concentration (C_t) was measured after 3 hours. As shown in Fig. 6(a) and Fig. S2, IVO-R achieved complete MB removal (100% efficiency) within 30 minutes, corresponding to an adsorption capacity of 47 mg g^{-1}. In contrast, IVO-S exhibited lower performance, adsorbing 66% of MB with a maximum capacity of 33 mg g^{-1}.

XPS data show that hydroxyl groups are present only on the surface of the IVO-S sample and absent on the IVO-R sample, where they may facilitate dye adsorption by acting as adsorption sites. However, despite the lack of confirmed hydroxyl groups, the IVO-R sample shows higher adsorption performance. The higher adsorption capacity of IVO-R compared with IVO-S indicates that hydroxyl-related groups are not the primary factor controlling MB uptake in this system. The superior performance of the rod-shaped IVO-R sample aligns with the SEM and TEM data, which show that it has a smaller particle size compared to the spherical IVO-S sample, therefore offering a larger surface area for adsorption. To better compare particle sizes, the equivalent spherical diameter (ESD) of the nanorods based on Eqn 10 was estimated.[52] Assuming a cylindrical geometry with an average width of 27 nm and length of 1000 nm (based on TEM images), the average volume (V) was calculated to be approximately 5.22×10^{-22} m^3. Using eqn (10), the ESD (d_e) was determined to be 103.02 nm, significantly smaller than the ~2000 nm diameter of the spherical sample. This substantial difference in particle size contributes to the enhanced adsorption performance of the rod-shaped morphology by providing more active surface area.

$$d_e = \left(\frac{6V}{\pi}\right)^{\frac{1}{3}} \quad (10)$$

These results demonstrate that different morphologies of $InVO_4$ function effectively as adsorbents in dye removal, rather than as photocatalysts. However, by optimizing the morphology, their adsorption capacity can be significantly enhanced.

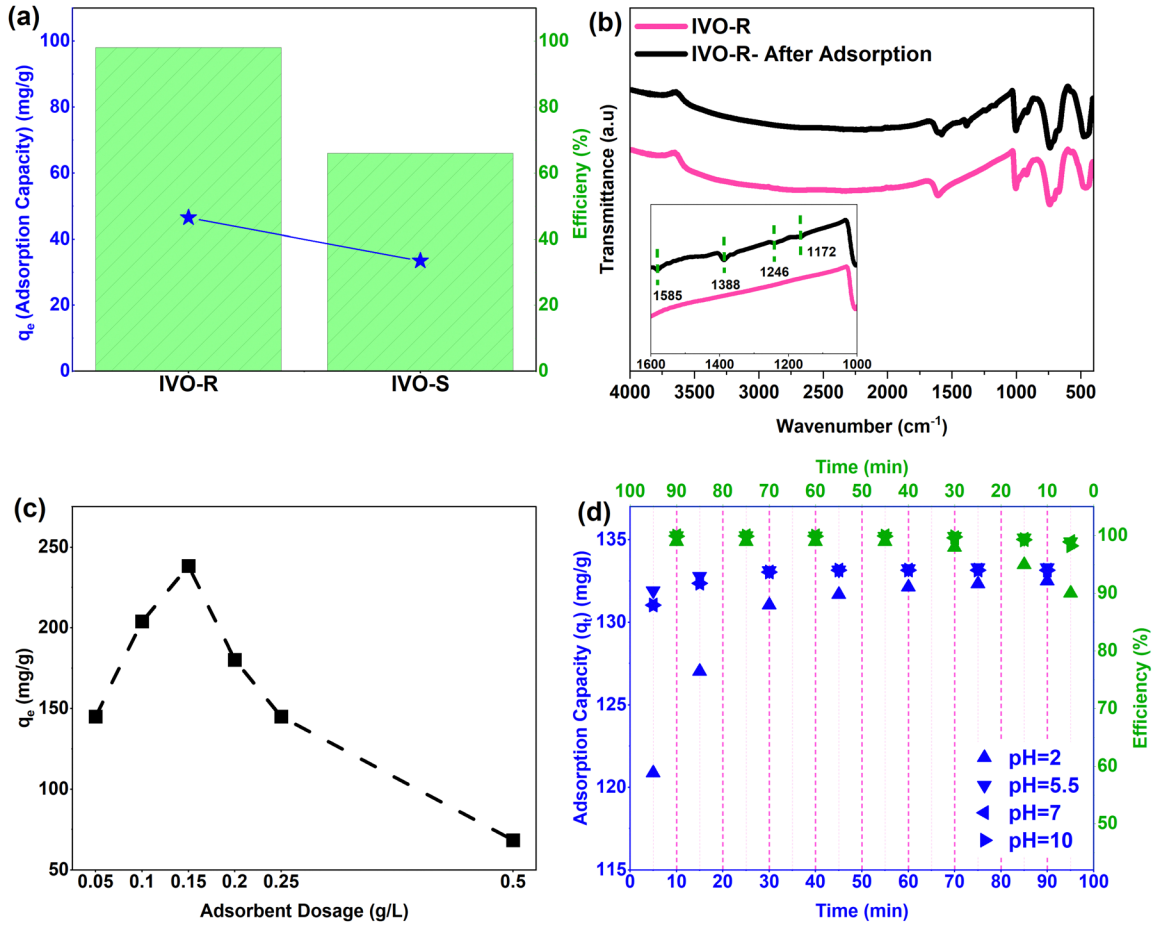

Fig. 6 (a) Comparison of adsorption capacity and efficiency of IVO-S and IVO-R samples (0.1 g L^{-1} adsorbent dosage, 5 mg L^{-1} MB concentration, experiment time: 3 h), (b) FTIR spectra of the IVO-R sample before and after adsorption test (0.1 g L^{-1} adsorbent dosage, 5 mg L^{-1} MB concentration), (c) effect of adsorbent (IVO-R) dosage on the adsorption capacity (40 mg L^{-1} MB concentration), and (d) effect of pH on adsorption capacity and MB adsorption efficiency (0.15 g L^{-1} adsorbent dosage, 20 mg L^{-1} MB concentration).

Based on the results shown in Fig. 6(a), the IVO-R sample with nanorod morphology was chosen as the optimized sample and selected for further investigation and enhancement of $InVO_4$ adsorption capacity.

To further investigate and confirm the adsorption of methylene blue (MB) on the surface of the IVO-R sample, FTIR measurements were performed before and after the adsorption test. As shown in Fig. 6(b), four new absorption bands appear in the FTIR spectrum of IVO-R after MB adsorption at 1172, 1246, 1388, and 1585 cm^{-1}, which are associated with MB molecules on the surface. The bands at 1172 and 1246 cm^{-1} correspond to N–CH_3 stretching vibrations.[53] Additionally, the peaks at 1585 and 1388 cm^{-1} are attributed to the C=C skeletal stretching of the benzene ring in the phenothiazine core and the C–N stretching vibration, respectively.[54] These characteristic organic vibrations, absent in the pristine IVO-R spectrum, confirm the successful adsorption of MB onto the IVO-R surface during the adsorption process.

Another key parameter for maximizing the adsorption capacity is the adsorbent dosage. To optimize this, the IVO-R sample (as the optimized morphology) was used in a series of experiments with varying dosages added to a 40 mg L^{-1} MB solution. The experiments were continued until an equilibrium concentration (C_e) was reached, and the adsorption capacity (q_e) was calculated for each dosage. As shown in Fig. 6(c), the highest adsorption capacity was achieved at a dosage of 0.15 g L^{-1}, reaching 239 mg g^{-1}. Although complete MB removal was not observed at lower dosages (*e.g.*, 0.05 and 0.1 g L^{-1}), these samples still exhibit high adsorption capacities of 145 and 204 mg g^{-1}, respectively. At and above 0.15 g L^{-1}, full MB adsorption occurs; however, a downward trend in q_e was observed beyond this dosage, as illustrated in Fig. 6(c). This decline is attributed to the saturation of available MB molecules relative to the excess adsorbent surface area. Therefore, 0.15 g L^{-1} is identified as the optimal dosage, balancing maximum adsorption efficiency with minimal adsorbent usage.

In addition, Fig. 6(d) illustrates the effect of pH on the adsorption of MB dye by the IVO-R sample. Experiments were conducted at four different pH values (2, 5.5, 7, and 10) using a fixed IVO-R dosage of 0.15 g L^{-1} and an MB concentration of 20 mg L^{-1}. Remarkably, complete dye removal (100% efficiency) was achieved across all pH conditions, indicating that

$InVO_4$ exhibits excellent pH tolerance and consistent adsorption performance in acidic, neutral, and basic environments. Although the final adsorption capacity was similar across all conditions, a slight difference in adsorption kinetics was observed at pH 2. While samples at pH 5.5, 7, and 10 reached full dye removal within the first 5 minutes, the pH 2 sample required up to 30 minutes to achieve complete adsorption. During the initial phase, the adsorption capacity of the pH 2 sample remained below 130 mg g^{-1}, whereas the other samples exceeded this value within 5 minutes. All samples reached equilibrium after 90 minutes, confirming that pH does not significantly affect the overall adsorption behavior of $InVO_4$.

This trend can be explained by measuring the surface charge of the IVO-R sample at different pH values. Fig. S3 shows the zeta potential of IVO-R in acidic and basic environments. The IVO-R sample exhibits a negative surface charge across the entire pH range (2–10) and as pH increases, the surface charge becomes more negative, from −10.82 mV at pH 2 to −118.27 mV at pH 10. MB predominantly exists in the cationic form (MB^+);[50] therefore, electrostatic attraction is the primary mechanism for adsorption, and the consistently negative surface charge of IVO-R explains its high adsorption rate and pH tolerance. However, under strongly acidic conditions (pH = 2), the adsorption rate is lower. This can be explained by the presence of excess H^+ ions and the less negative surface potential at this pH compared to that at higher pH values. At higher pH levels (5.5–10), the adsorption process follows a very similar trend. After optimizing different parameters, the IVO-R sample exhibited a maximum adsorption capacity of 290 mg g^{-1}, which is comparable to that of conventional adsorbents. The performance of $InVO_4$ as an adsorbent obtained in this study is compared with the conventional adsorbents, shown in Table S2.

These findings suggest that $InVO_4$ maintains strong adsorption performance across a wide pH range, making it highly versatile for practical applications. Moreover, due to its consistently high adsorption efficiency, adjusting the pH to avoid adsorption and isolate photocatalytic degradation is not feasible. This supports the conclusion that dye removal by $InVO_4$ is dominated by adsorption rather than photocatalysis.

To further evaluate the adsorption performance of $InVO_4$, its behavior toward mixed pollutants was also investigated, as shown in Fig. S4. A binary dye mixture containing RhB and MB in equal proportions (1 : 1) was prepared, with each dye at a concentration of 20 mg L^{-1}, resulting in a total pollutant concentration of 40 mg L^{-1}. It can be observed that the absorption peak at 664 nm, corresponding to MB, disappears within the first 5 minutes. Nevertheless, the characteristic peak of RhB at 554 nm remains visible even after 180 minutes of the reaction, and the removal efficiency for rhodamine B in the mixed solution is approximately 60%. The color of the mixed pollutant solution changes from violet to pink, indicating the presence of residual rhodamine B in the solution (Fig. S5).

To investigate the adsorption kinetics and rate of MB removal by IVO-R, experimental data at two initial MB concentrations (30 and 50 mg L^{-1}) were fitted to the pseudo-first order (PFO) and pseudo-second order (PSO) models. Since linearized forms of these models often introduce error propagation, a nonlinear fitting approach was employed for greater accuracy, as shown in Fig. 7(a). The corresponding rate constants and R^2 values are summarized in Table 2. Both PFO and PSO models are derived from simplified Langmuir kinetics and exhibit dependence on the initial concentration (C_0).[55,56] Typically, PFO describes an adsorption well at high C_0, the initial stage of adsorption and when few active sites are available, whereas PSO provides a better fit at low C_0 and when adsorption occurs at final stages and the surface is abundant with active sites.[57–59] Based on the obtained parameters, the PSO model demonstrates better correlation with the experimental data for both concentrations, with R^2 values of 0.999 (MB30) and 0.987 (MB50), compared to 0.997 (MB30) and 0.972 (MB50) for PFO. This observation aligns with previous studies, which report that

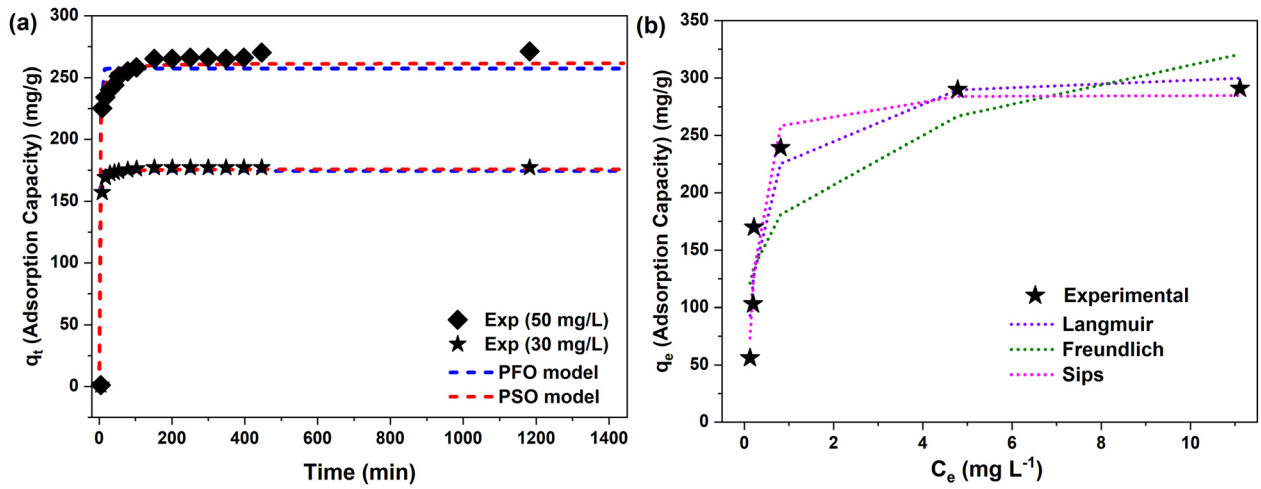

Fig. 7 (a) Adsorption kinetics of MB at two different concentrations (30 and 50 mg L^{-1}) by the IVO-R sample and fitting with PFO and PSO models, and (b) adsorption isotherm study with Langmuir, Freundlich, and Sips (IVO-R sample, 0.15 g L^{-1} adsorbent dosage concentration, T = room temperature, time: 24 h).

Table 2 Adsorption kinetic rate constant and R^2 value for pseudo-first order and pseodo-second order models applied to the adsorption of MB (30 and 50 mg L^{-1}) by the IVO-R sample

MB initial concentration (mg L^{-1})	Pseudo first-order model					Pseudo second-order model				
	K_1 (min^{-1})	R^2	$(q_e)_{exp}$ (mg g^{-1})	$(q_e)_{act}$	RMSE (mg g^{-1})	K_2 (g mg^{-1} min^{-1})	R^2	$(q_e)_{exp}$ (mg g^{-1})	$(q_e)_{act}$	RMSE (mg g^{-1})
50	0.401	0.972	257.42	270.18	10.54	0.003	0.987	261.63	270.18	7.23
30	0.448	0.997	174.39	175.69	2.22	0.009	0.999	175.87	175.69	0.65

adsorption at low adsorbate concentrations generally follows second-order kinetics.[59] The adsoprtion of MB by the IVO-R sample and the change in the color also is shown in Fig. S6.

The PSO rate constant (k_2) was higher at lower MB concentration (0.009 g mg^{-1} min^{-1} for MB30) than at higher concentration (0.003 g mg^{-1} min^{-1} for MB50), indicating faster adsorption at lower dye concentrations. This difference can be attributed to the greater availability of active sites relative to dye molecules at lower concentrations. At MB30, the PSO-predicted adsorption capacity (175.87 g mg^{-1}) closely matched the experimental value (175.69 g mg^{-1}), whereas at MB50, the deviation between predicted and actual values increases slightly, reflecting the effect of site saturation at higher concentrations.

After evaluating the adsorption rate through kinetic studies, it is essential to examine the interaction between the adsorbent and adsorbate at equilibrium. To achieve this, adsorption isotherm studies were performed using three models: Langmuir, Freundlich, and Sips. The Langmuir model assumes monolayer adsorption on a homogeneous surface without interaction between adsorbed molecules, whereas the Freundlich model describes adsorption on a heterogeneous surface with the possibility of multilayer formation.[60] The Sips model combines features of both Langmuir and Freundlich models, and it can account for surface heterogeneity and effectively overcome the limitations of the Langmuir and Freundlich models, particularly at higher adsorbate concentrations. The optimized IVO-R sample was used for isotherm studies with varying MB concentrations. Experimental data and model fittings are presented in Fig. 7(b), and the corresponding parameters including predicted maximum adsorption capacity, R^2, and error metrics (ARE and RMSE) are summarized in Table 3. As the initial dye concentration increased, the maximum adsorption capacity also increased until reaching equilibrium at approximately 50 mg L^{-1}. Based on R^2 values, the experimental data exhibit the best fit with the Sips model (R^2 = 0.95), which predicts a maximum adsorption capacity of 285 mg g^{-1}, very close to the experimental value (290 mg g^{-1}). Additionally, the Langmuir model provides a better correlation than the Freundlich model, with higher R^2 and lower error values. The Langmuir-predicted capacity (308 mg g^{-1}) is also close to the experimental result. These findings, combined with the observed plateau in adsorption capacity and the non-porous nature of the samples, suggest that MB molecules primarily form a monolayer on the heterogeneous surface of IVO-R, which contains non-uniform active sites. In addition, the

Table 3 Isotherm model-predicted maximum adsorption capacity, R^2, ARE and RMSE values

Adsorption model	Parameters		Obtained values
Langmuir	q_m	(mg g^{-1})	307.85
	b	(L mg^{-1})	3.36
	R^2		0.92
	ARE	(%)	19.62
	RMSE	(mg g^{-1})	24.77
Freundlich	K_F	(mg g^{-1}) (L mg^{-1})$^{1/n}$	189.50
	n		4.58
	R^2		0.77
	ARE	(%)	34.66
	RMSE	(mg g^{-1})	43.00
Sips	q_m	(mg g^{-1})	285.14
	K_s	(L mg^{-1})	4.31
	n		1.81
	R^2		0.95
	ARE	(%)	13.74
	RMSE	(mg g^{-1})	20.24

obtained n value of 1.81 for the Sips model suggests that MB adsorption occurs on the heterogeneous IVO-R surface with non-uniform adsorption affinities. This heterogeneity is consistent with the nanorod morphology of IVO-R, where different exposed facets, edge/corner sites, defect sites, and local surface-charge environments may provide adsorption sites with different affinities toward MB.

3.1. Mechanistic study

The adsorption mechanism was investigated using FTIR, zeta potential, and XPS analyses. Zeta potential measurements (Fig. 6e) revealed that the IVO-R sample possesses negatively charged surfaces and exhibits significant adsorption only for cationic dyes (MB and RhB) suggesting that electrostatic interactions play a dominant role in the adsorption process. FTIR spectra provide further evidence of MB adsorption on the $InVO_4$ surface, because four additional peaks appear in the spectrum of the IVO-R sample following adsorption (Fig. 6b). In contrast, XPS analysis of IVO-R before and after dye adsorption (Figure S7) shows no discernible changes in peak positions or oxidation states, indicating the absence of strong chemical bonding between the MB molecules and the $InVO_4$ surface. While the adsorbent is inorganic, V–O–V and In–O–V linkages may act as electron-rich regions that could potentially interact with the aromatic rings of the dye *via* π–π interactions. However, the presence of π–π stacking cannot be conclusively demonstrated based on the available data and is therefore proposed only as a possible interaction mechanism. This

observation implies that non-covalent interactions control the adsorption process. The comparative adsorption performance for MB and RhB further supports this interpretation: although both dyes are cationic and subject to electrostatic attraction, the IVO-R sample exhibits higher adsorption for MB. This difference can be attributed to the simpler, planar structure of MB, which facilitates stacking with $InVO_4$ rods more effectively than the bulkier RhB molecules, thereby enhancing the adsorption capacity for MB (Table S1).

4. Conclusion

To conclude, although both $InVO_4$ morphologies exhibit narrow band gaps ($\sim$2.4 eV), dye removal occurs predominantly through adsorption rather than photocatalytic degradation. This is evidenced by comparable removal efficiencies under light and dark conditions, confirming adsorption as the primary mechanism. Among the two morphologies, the nanorod structure (IVO-R) demonstrates superior adsorption capacity compared to the spherical form, achieving a maximum capacity of 290 mg g^{-1} for MB. The IVO-R sample also exhibits excellent pH tolerance, maintaining high adsorption performance across a wide pH range (2–10), with only a slight initial rate reduction under highly acidic conditions due to lower zeta potential and H^+ competition. $InVO_4$ shows a strong preference for cationic dyes, while adsorption of anionic dyes such as MO is negligible. This behavior is attributed to electrostatic attraction between the negatively charged surface and cationic dye molecules. Furthermore, although FTIR confirms the presence of MB molecules on the surface of $InVO_4$, the XPS results indicate the absence of strong chemical bonding between MB and the $InVO_4$ surface, suggesting that adsorption occurs *via* non-covalent interactions between the MB molecule and the $InVO_4$ surface. Kinetic studies confirm that adsorption follows a pseudo-second order (PSO) model, with rate constants (k_2) of 0.003 and 0.009 g mg^{-1} min^{-1} for MB concentrations of 50 and 30 mg L^{-1}, respectively. Isotherm analysis reveals that the Sips model provides the best fit, indicating monolayer adsorption on a heterogeneous surface with non-uniform active sites.

Author contributions

H. E.: conceptualization, investigation, visualization, formal analysis, methodology, data curation, and writing – original draft. R. I.: investigation, visualization, and data curation. A. A.: investigation, visualization, and data curation. A. D.: conceptualization, supervision, literature survey, data curation, formal analysis, and writing – review & editing. M. E. C.: data curation, formal analysis, and writing – review & editing. D. C. L.: conceptualization, supervision, project administration, and funding acquisition.

Conflicts of interest

There are no conflicts to declare.

Data availability

The data that support the findings of this study are available from the corresponding authors upon reasonable request.

Supplementary information (SI) is available. See DOI: https://doi.org/10.1039/d6ma00355a.

Acknowledgements

H. Esmaili is grateful for the financial support from the German Academic Exchange Service (DAAD) for this project. A. Dubey is grateful for the DAAD-postdoctoral PRIME funding. Also, the authors thank Prof. Matthias Epple's research group and Shaista Tahir for FTIR measurements and also Dr Ulrich Hagemann for XPS measurements. Christoph Ochsendorf, Prof. Selina Olthof, Maryam Choghaei, Witchaya Arpavate, Young Un Jin and Dr Mahmoud Mazarji are acknowledged for their scientific discussions.

References

1 M. T. Yagub, T. K. Sen, S. Afroze and H. M. Ang, *Adv. Colloid Interface Sci.*, 2014, **209**, 172–184.
2 V. Katheresan, J. Kansedo and S. Y. Lau, *J. Environ. Chem. Eng.*, 2018, **6**, 4676–4697.
3 T. Robinson, G. McMullan, R. Marchant and P. Nigam, *Bioresour. Technol.*, 2001, **77**, 247–255.
4 Y. Deng and R. Zhao, *Curr. Pollut. Rep.*, 2015, **1**, 167–176.
5 R. Dewil, D. Mantzavinos, I. Poulios and M. A. Rodrigo, *J. Environ. Manage.*, 2017, **195**, 93–99.
6 A. Maleki, A. H. Mahvi, R. Ebrahimi and Y. Zandsalimi, *Korean J. Chem. Eng.*, 2010, **27**, 1805–1810.
7 S. Y. Tee, J. Kong, J. J. Koh, C. P. Teng, X. Wang, X. Wang, S. L. Teo, W. Thitsartarn, M.-Y. Han and Z. W. Seh, *Nanoscale*, 2024, **16**, 18165–18212.
8 M. Mazarji, B. Aminzadeh, M. Baghdadi and A. Bhatnagar, *J. Mol. Liq.*, 2017, **233**, 139–148.
9 K. K. Choy, G. McKay and J. F. Porter, *Resour., Conserv. Recycl.*, 1999, **27**, 57–71.
10 F. Mcyotto, Q. Wei, D. K. Macharia, M. Huang, C. Shen and C. W. Chow, *Chem. Eng. J.*, 2021, **405**, 126674.
11 A. Szyguła, E. Guibal, M. A. Palacín, M. Ruiz and A. M. Sastre, *J. Environ. Manage.*, 2009, **90**, 2979–2986.
12 S. S. Moghaddam, M. A. Moghaddam and M. Arami, *J. Hazard. Mater.*, 2010, **175**, 651–657.
13 A. Haleem, A. Shafiq, S.-Q. Chen and M. Nazar, *Molecules*, 2023, **28**, 1081.
14 J. J. Rueda-Marquez, I. Levchuk, P. F. Ibañez and M. Sillanpää, *J. Cleaner Prod.*, 2020, **258**, 120694.
15 H. Fu, S. Zhang, T. Xu, Y. Zhu and J. Chen, *Environ. Sci. Technol.*, 2008, **42**, 2085–2091.
16 R. F. de Luis, A. Martinez-Amesti, E. S. Larrea, L. Lezama, A. T. Aguayo and M. I. Arriortua, *J. Mater. Chem. A*, 2015, **3**, 19996–20012.
17 M. Simić, J. Petrović, M. Koprivica, M. Ercegović, J. Dimitrijević, N. S. Vuković and N. Fiol, *Toxics*, 2025, **13**, 459.

18 G. Crini, *Bioresour. Technol.*, 2006, **97**, 1061–1085.
19 M. Ahmaruzzaman, S. Roy, A. Singha, S. Rtimi and T. M. Aminabhavi, *Adsorption*, 2025, **31**, 34.
20 F. Fresno, R. Portela, S. Suárez and J. M. Coronado, *J. Mater. Chem. A*, 2014, **2**, 2863–2884.
21 I. Ahmad, G. Li, A. Al-Qattan, A. J. Obaidullah, A. Mahal, M. Duan, K. Ali, Y. Y. Ghadi and I. Ali, *Mater. Today Sustainability*, 2024, **25**, 100666.
22 P. Dhull, A. Sudhaik, V. Sharma, P. Raizada, V. Hasija, N. Gupta, T. Ahamad, V. Nguyen, A. Kim, M. Shokouhimehr, S. Y. Kim, Q. Van Le and P. Singh, *Mol. Catal.*, 2023, 539.
23 T. H. Noh, D. W. Kim, S. W. Seo, I. S. Cho, D. H. Kim, H. S. Han and K. S. Hong, *Mater. Lett.*, 2012, **72**, 98–100.
24 Y. X. Zhang, D. Ma, J. Wu, Q. Z. Zhang, Y. J. Xin and N. Bao, *Appl. Surf. Sci.*, 2015, **353**, 1260–1268.
25 Q. H. Shen, Z. Y. You, Y. Yu, T. Qin, Y. X. Su, H. Wang, C. C. Wu, F. Zhang and H. Yang, *Eur. J. Inorg. Chem.*, 2018, 1080–1086.
26 W. L. Shi, F. Guo, J. B. Chen, G. B. Che and X. Lin, *J. Alloys Compd.*, 2014, **612**, 143–148.
27 J. C. Shen, H. Yang, Y. Feng, Q. F. Cai and Q. H. Shen, *Solid State Sci.*, 2014, **32**, 8–12.
28 D. Mitoraj, U. Lamdab, W. Kangwansupamonkon, M. Pacia, W. Macyk, N. Wetchakun and R. Beranek, *J. Photochem. Photobiol., A*, 2018, **366**, 103–110.
29 U. Lamdab, K. Wetchakun, S. Phanichphant, W. Kangwansupamonkon and N. Wetchakun, *Catal. Today*, 2016, **278**, 291–302.
30 Y. Wang, H. X. Dai, J. G. Deng, Y. X. Liu, H. Arandiyan, X. W. Li, B. Z. Gao and S. H. Xie, *Solid State Sci.*, 2013, **24**, 62–70.
31 K. M. Ji, J. G. Deng, H. J. Zang, J. H. Han, H. Arandiyan and H. X. Dai, *Appl. Catal., B*, 2015, **165**, 285–295.
32 N. Wetchakun, P. Wanwaen, S. Phanichphant and K. Wetchakun, *RSC Adv.*, 2017, **7**, 13911–13918.
33 Y.-P. Huang, H.-B. Niu, L. Jin, L. Jiao, D. Johnson, H.-L. Tian, S. Sarina, H.-Y. Zhu and Y.-F. Fang, *Chem. Eng. J. Adv.*, 2023, **15**, 100508.
34 H. Feng, Y. N. Liang, C. P. Hu and X. Hu, *Sep. Purif. Technol.*, 2022, 293.
35 S. Lagergren, *Kungl. Svenska Vetenskapsakad. Handl.*, 1898, **24**, 1–39.
36 Y.-S. Ho and G. McKay, *Process Biochem.*, 1999, **34**, 451–465.
37 I. Langmuir, *J. Am. Chem. Soc.*, 1918, **40**, 1361–1403.
38 H. Freundlich, *Z. Phys. Chem.*, 1907, **57**, 385–470.
39 R. Sips, *J. Chem. Phys.*, 1948, **16**, 490–495.
40 H. Zhang, X. Lv, Y. Li, Y. Wang and J. Li, *ACS Nano*, 2010, **4**, 380–386.
41 W. Gao, C. Ran, M. Wang, L. Li, Z. Sun and X. Yao, *Phys. Chem. Chem. Phys.*, 2016, **18**, 18219–18226.
42 Y. Zhu, Y. Wang, W. Yao, R. Zong and Y. Zhu, *RSC Adv.*, 2015, **5**, 29201–29208.
43 S. Cipagauta-Diaz, A. Estrella-González and R. Gomez, *Mater. Sci. Semicond. Process.*, 2019, **89**, 201–211.
44 H. Y. Hafeez, A. D. G. Kafadi, J. Mohammed, A. B. Suleiman, C. E. Ndikilar, R. S. Sa'id, I. Muhammad and F. K. Alharbi, *J. Sol-Gel Sci. Technol.*, 2025, 1–9.
45 F. Y. Chen, L. Cheng, Y. B. Tang, K. K. Shu and W. L. Shi, *J. Chem. Technol. Biotechnol.*, 2021, **96**, 3074–3083.
46 P. Makuła, M. Pacia and W. Macyk, *J. Phys. Chem. Lett.*, 2018, **9**, 6814–6817.
47 G. P. López, D. G. Castner and B. D. Ratner, *Surf. Interface Anal.*, 1991, **17**, 267–272.
48 E. McCafferty and J. Wightman, *Surf. Interface Anal.*, 1998, **26**, 549–564.
49 K. M. Nguyen, A. V. Phan, N. T. Dang, T. Q. Tran, H. K. Duong, H. N. Nguyen and M. V. Nguyen, *Mater. Adv.*, 2023, **4**, 2636–2647.
50 J.-C. Bollinger, E. C. Lima, L. Mouni, S. Salvestrini and H. N. Tran, *Environ. Chem. Lett.*, 2025, 1–22.
51 A. Bekhoukh, I. Moulefera, F. Z. Zeggai, A. Benyoucef and K. Bachari, *J. Polym. Environ.*, 2022, **30**, 886–895.
52 B. Jennings and K. Parslow, *Proc. R. Soc. A*, 1988, **419**, 137–149.
53 A. Xu, X. Li, S. Ye, G. Yin and Q. Zeng, *Appl. Catal., B*, 2011, **102**, 37–43.
54 X. Teng, J. Li, Z. Wang, Z. Wei, C. Chen, K. Du, C. Zhao, G. Yang and Y. Li, *RSC Adv.*, 2020, **10**, 24712–24720.
55 S. Azizian, *J. Colloid Interface Sci.*, 2004, **276**, 47–52.
56 Y. Liu and L. Shen, *Langmuir*, 2008, **24**, 11625–11630.
57 H.-D. Choi, W.-S. Jung, J.-M. Cho, B.-G. Ryu, J.-S. Yang and K. Baek, *J. Hazard. Mater.*, 2009, **166**, 642–646.
58 T. Iida, Y. Amano, M. Machida and F. Imazeki, *Chem. Pharm. Bull.*, 2013, **61**, 1173–1177.
59 J. Wang and X. Guo, *J. Hazard. Mater.*, 2020, **390**, 122156.
60 M. A. Al-Ghouti and D. A. Da'ana, *J. Hazard. Mater.*, 2020, **393**, 122383.